Available online at www.sciencedirect.com
ScienceDirect
Earth and Planetary Science Letters 257 (2007) 132 – 145
EPSL
www.elsevier.com/locate/epsl

Physical controls on the salinity of mid-ocean ridge hydrothermal vent fluids

Fabrice J. Fontaine [a,*], William S.D. Wilcock [a], David A. Butterfield [b]

[a] University of Washington, School of Oceanography, Box 357940, Seattle WA 98195-7940, United States
[b] University of Washington, Joint Institute for the Study of the Atmosphere and Oceans, 7600 Sand Point Way NE, Seattle WA 98115, United States

Received 12 September 2006; received in revised form 2 February 2007; accepted 15 February 2007
Available online 23 February 2007
Editor: H. Elderfield

Abstract

Variations in the salinity of black smoker effluents (0.1–∼8 wt.% NaCl) relative to seawater (3.2 wt.% NaCl) are attributed to phase separation and segregation of the resulting brines and vapors. However, models of phase separation predict brines with substantially higher salinities than observed at vents and such brines are commonly observed in fluid inclusions from fossil hydrothermal systems. It has been postulated that the range of observed salinities is controlled by the density of upwelling fluids. Here we present models of hydrothermal circulation that predict the observed maximum salinity when an upper layer of high-permeability is included, and also reproduce black smoker temperatures when the upflow zone is surrounded by a low-permeability shell. Pressure gradients across the permeability boundary act as a density filter impeding the passage of high-salinity fluids, while the shell provides sufficient insulation to tap hot fluids to the surface. Our models fit the observations when the permeabilities of the upper layer differ from the permeability of the lower layer by factors of ∼10 and ∼100 in upflow and downflow regions, respectively, and when the permeability of the shell is one tenth that of the lower layer. The permeability structure we propose is consistent with observations in oceanic crust and inferences from ophiolites. While a previous study argues that black smoker temperatures are a consequence of the thermodynamic properties of seawater, our work suggests that very specific permeability configurations are required to match both the temperature and maximum salinity.

Keywords: hydrothermal systems; mid-ocean ridges; salinity; numerical modeling

1. Introduction

The discrepancy between the conductive heat flux measured near mid-ocean ridges and that predicted by models of conductive cooling of the oceanic lithosphere is a result of extensive hydrothermal heat transport across the seafloor [1–3]. For plate ages < ∼1-Ma hydrothermal circulation accounts for ∼10% of the total heat loss from the earth [4]. The most vigorous hydrothermal cells are found on the ridge axis and are driven by the heat extracted from crustal magma chambers. Seawater penetrates the fractured oceanic crust in recharge areas and is progressively heated as it moves down in the pillow lavas and sheeted dike complex (Fig. 1a). These fluids reach chemical equilibrium at ∼400–450 °C in a high-temperature reaction zone at the base of the sheeted dike complex

---

* Corresponding author. Now at: Institut de Physique du Globe, Equipe de Géosciences Marines, Boite 89, 4 place Jussieu, 75252 Paris Cedex 05, France. Tel.: +33 1 44 27 50 88; fax: +33 1 44 27 99 69.
E-mail address: fontaine@ipgp.jussieu.fr (F.J. Fontaine).

0012-821X/$ - see front matter © 2007 Elsevier B.V. All rights reserved.
doi:10.1016/j.epsl.2007.02.027

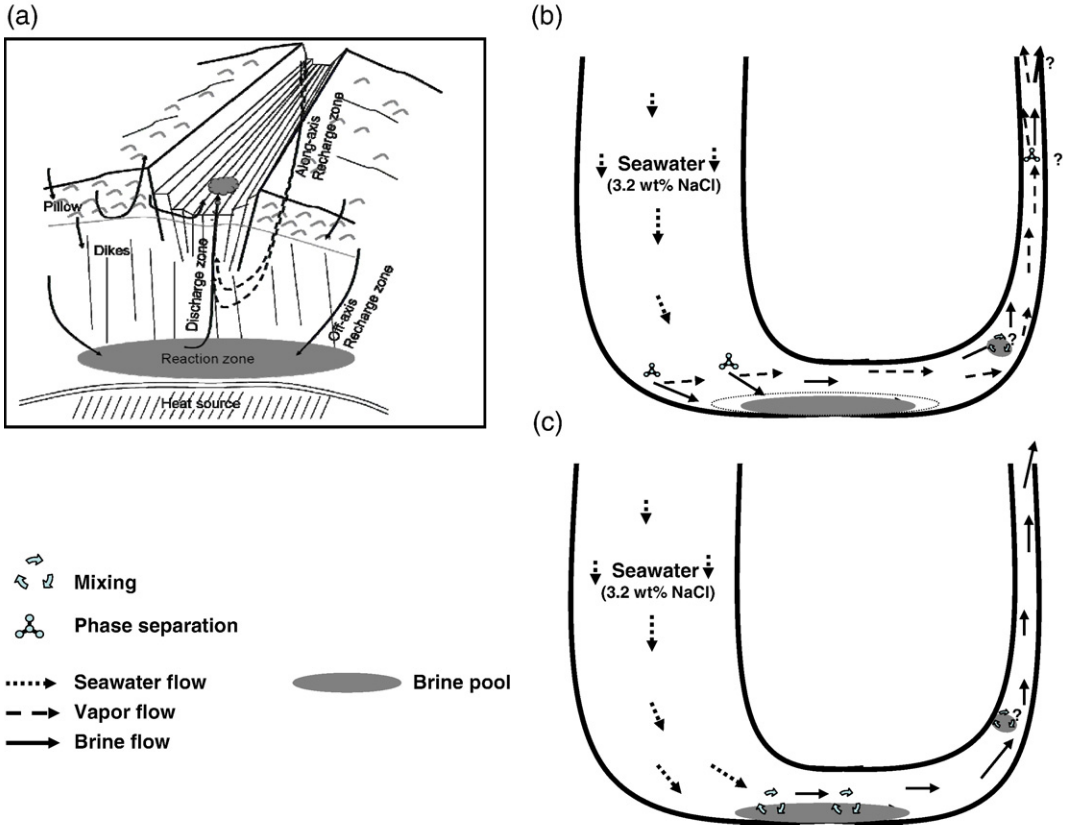

Fig. 1. (a) Cartoon illustrating the architecture of mid-ocean ridge hydrothermal system (after Alt [63]). (b) Conceptual pipe-flow models for mid-ocean ridge hydrothermal systems. Seawater downwells in the recharge zone and phase-separates in the super-critical reaction zone producing a low-buoyancy brine and a high-buoyancy vapor. While vapor rises in the upflow zone, brines are stored in-situ or rise only slowly [20]. Depending on the pressure and temperature conditions in the upflow zone, the low-salinity vapor may (i) vent directly at the seafloor or (ii) undergo further phase separation in the upflow zone to feed low- and high-salinity vents. (c) The reaction zone has returned to the single-phase area. Seawater mixes with brines producing higher-salinity fluids that upwell and vent at the seafloor.

before rising in discharge zones to vent at the seafloor [e.g., [5,6]]. Hydrothermal fluids vent either in focused high-temperature smokers or in lower-temperature diffuse vents. Diffuse vents result from a combination of mixing cold seawater with a high-temperature end member [e.g., [7,8]] and the conductive heating of seawater in the shallow crust [e.g., [9]].

To date, nearly 300 sites of venting have been inferred along the ridge axis, of which ~150 have been visited [10]. Fluid sampling studies have led to an extensive dataset of venting temperature and fluid chemistry. The observed smoker temperatures range from ~200 °C to just over 400 °C with the majority concentrated between 320 °C and 380 °C (Fig. 2a). Jupp and Schultz [11] show that the thermodynamic properties of seawater maximize heat transport near 400 °C and thus argue that the observed maximum temperature can be explained independently of the permeability structure or details of hydrothermal flow patterns.

A primary characteristic of the fluid samples is that they are either depleted or enriched in salt (chloride, Cl) compared to seawater (3.2 wt.% NaCl) [12,13]. Venting salinities range from 5% to >200% of the seawater value with only a handful of salinities exceeding 5.5 wt.% NaCl (Fig. 2a). It has been accepted since the late 1980s that salinity variations are a result of phase separation followed by the segregation of the vapor and brine phases [14–17]. In a few systems sub-critical phase separation at shallow depths is important [e.g., [18]] and this process can account for the very low salinities observed in some samples with the highest temperatures close to 400 °C (see Fig. 2a). However, in most systems the observed salinity variations are attributed to super-critical phase separation near the base of the hydrothermal cell [e.g., [19]].

Although phase separation can account for the deviation of salinities from seawater values, it is insufficient to explain why maximum observed salinities are

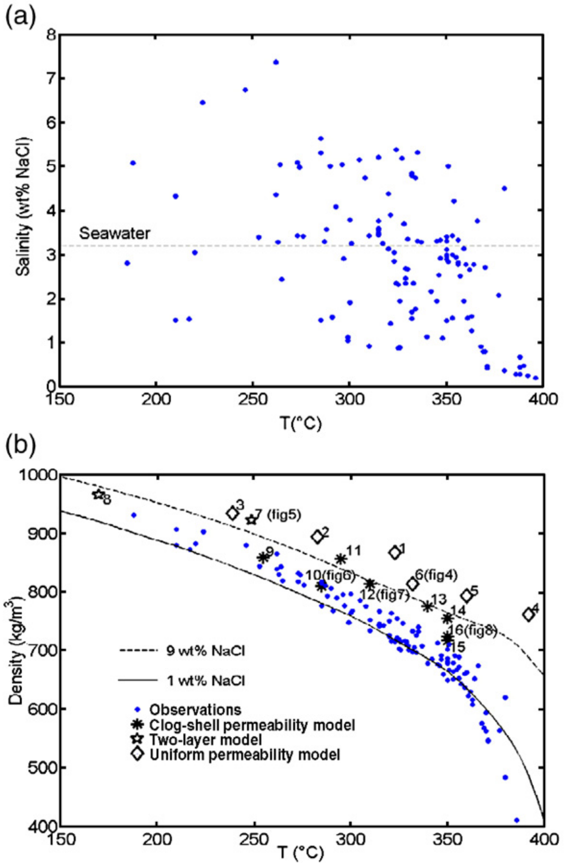

Fig. 2. (a) Global high-temperature vents salinity versus temperature. Maximum venting salinities are limited to 5–8 wt.% NaCl. Data are from VonDamm [12] and Butterfield et al. [13]. (b) Venting density versus temperature for the global dataset shown in (a) (dots). Venting densities predicted by our numerical experiments are also plotted for models with a uniform permeability (diamonds), a layered permeability (stars) and a clog-shell permeability structure (asterisks) (see Fig. 3). The densities of fluids with 1 and 9 wt.% NaCl at $P = 300$ bars are also shown. Numbers refer to model numbers in Table 1. The models shown in this paper are labeled with the figure number.

limited to about 5 to 8 wt.% NaCl, without additional reference to the physics of whether fluids will rise through the system. At super-critical conditions, phase separation should lead to the formation of brines with salinities that increase with depth and may reach ~60 wt.% NaCl at 500 bars and 600 °C [20,21]. Fluid inclusion data recovered in ophiolites [e.g., [22,23]] and oceanic crustal sections [e.g., [24,25]] show that brines with salinities up to 60–70 wt.% NaCl do exist in the deepest parts of the system. At shallower depths, fluid inclusions from upflow zones have lower salinities [e.g., [26]] but the maximum values of 11–13 wt.% NaCl are about twice the maximum venting salinities [14,22].

It has been postulated that the range of observed salinities is controlled by their densities [20,27]. McNabb and Fenner [27] argue that at pressures typical of the base of mid-ocean ridge hydrothermal systems (400–500 bars) fluids with salinities >35 wt.% NaCl have densities >1000 kg/m^3 and are too dense to rise in the system. They conclude that layers of brine should form at the base of active systems. Bischoff and Rosenbauer [17] build upon these ideas to develop a two-layer model of circulation in which a single-pass seawater cell overlies a re-circulating brine layer. More recently, Fontaine and Wilcock [20] question the two-layer model. They suggest that the brines preferentially enter into the backwater porosity (i.e., the porosity that is poorly connected to the widest through going cracks that account for most of the flow), but do not form a separate layer. They argue that pressure gradients are likely close to cold hydrostatic in mid-ocean ridge hydrothermal systems and that brines with salinities up to 20–25 wt.% NaCl may be buoyant enough to move up in the upflow zone rather than being stored in a deep layer [20]. To account for vent salinities, they postulate that the permeability interface between the pillow and dike layers acts as a filter impeding the rise of high-salinity fluids.

In this work we explore this idea using single-phase, two-dimensional numerical models of hydrothermal circulation with realistic fluid properties and differing bottom temperatures, Nusselt numbers and permeability structures to investigate the physical controls on maximum venting salinities. We show that the venting salinity is dependent on the permeability structure and that the simplest models with uniform or layered permeability are unable to account for both the maximum observed salinity and temperature. We explore a more complex model in which the upflow is surrounded by a low-permeability shell and infer that such models are more consistent with the observational data.

2. Physical model

2.1. Transport direction

It is generally accepted that the large scale fluid circulation in the fissured oceanic crust can be described by Darcy's law [e.g., [28]]. Because hydrothermal fluids can phase-separate, this law has been extended to account for the two-phase flow of vapor and brine [28–32] yielding

$$\boldsymbol{q}_i = -\frac{k_i}{\mu_i}(\nabla P - \rho_i \boldsymbol{g}) \tag{1}$$

where subscript i refers to phase (v or b for vapor and brine, respectively), $\boldsymbol{q}_i$ is the Darcy velocity, $\boldsymbol{g}$ is the gravity

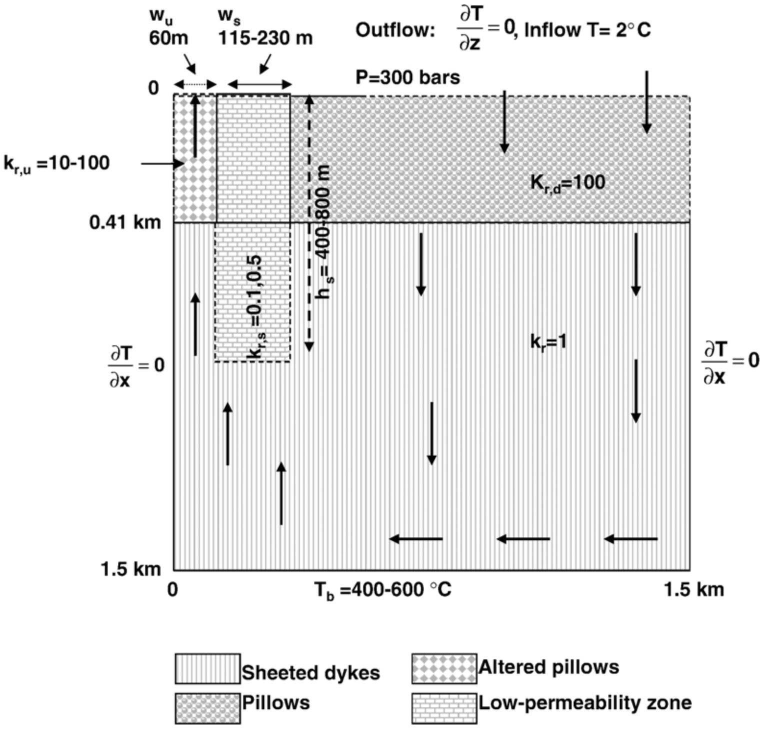

Fig. 3. Configuration of the two-dimensional models used for this study. For the clogged-shell model, a low-permeability zone separates upflow from downflow. The top of the system is still more permeable than the bottom, but the contrast may differ in zones of upflow and downflow. This permeability structure is consistent with observations from ophiolites [50] and previous modeling studies [49,54]. T_b is the basal temperature. $k_{r,d}$ and $k_{r,u}$ refer to the permeability of the top downflow and upflow area relative to the permeability of the bottom area ($k_r=1$). $k_{r,s}$ refers to the relative permeability of the low-permeability zone between the downflow and upflow zones. w_s and h_s refer to the width and height of the low-permeability shell, respectively. w_u is the thickness of the upflow zone. Boundary conditions for the numerical experiments are also shown.

vector, P is the total pressure, ρ_i is the density and μ_i is the viscosity. k_i is the effective permeability of phase i and is generally less than the intrinsic permeability [20]. The permeability reduction results from the coexistence of the two phases in the fractured basaltic matrix. The flow of each of them will be impeded by the presence of the other. When only one phase is present in the system, the effective permeability of the single phase reduces to the intrinsic permeability k ($k_i=k$).

It is generally accepted that the hydrothermal circulation at unsedimented mid-ocean ridges occurs in a single pass system in which the flow is near vertical everywhere except near the base of the system [33]. The direction of the vertical flows is governed by the balance between the total vertical pressure gradient and the product $\rho_i \boldsymbol{g}$ (see Eq. (1)) and satisfies

$$\begin{aligned} &\frac{1}{\boldsymbol{g}}\frac{\partial p}{\partial z} > \rho_i, \text{ upward fluid movement} \\ &\frac{1}{\boldsymbol{g}}\frac{\partial p}{\partial z} < \rho_i, \text{ downward fluid movement} \end{aligned} \qquad (2)$$

where the term $\frac{1}{\boldsymbol{g}}\frac{\partial p}{\partial z}$ represents the local neutral density.

In the mid-ocean ridge systems, the densities of venting fluids place a lower bound on the neutral densities in the underlying upflow zone. In Fig. 2b, we show these densities as a function of temperatures for the global dataset shown in Fig. 2a. We use the equation of state developed by Berndt et al. [34] for the system H_2O–NaCl to derive venting densities from the temperature, pressure and salinity dataset. Venting densities decrease roughly linearly from ~900 kg/m^3 at 200 °C to ~675 kg/m^3 at 350 °C. At higher temperatures venting densities decrease quickly with increasing temperatures and fluids venting at 380–400 °C have densities <500 kg/m^3. This pattern is due to the non-linear dependence of densities on temperature and pressure as the conditions approach the phase boundary.

2.2. Numerical investigations of neutral densities

According to Eq. (2), the value of the neutral density at any depth in the upflow zone provides an upper bound on the maximum density of rising fluids. In order to assess the spatial distribution of neutral densities, we ran a series of two-dimensional numerical models of hydrothermal circulation that build upon the work of Wilcock [35], Jupp and Schultz [36] and Fontaine and Wilcock [20]. The models are single-phase and do not include the phase separation of seawater and the segregation of the vapor and brine phases. In the two-phase area we followed the approach adopted by Wilcock [37] and we assume that the density is that of the two-phase mixture (i.e., sum of the density of each phase multiplied by the volume fraction it occupies) and that the viscosity is that of the volumetrically dominated phase. This approach is presumably accurate at least when a relatively small amount of brine is present in the system and should provide a reasonable approximation to flow in a single-phase upflow zone overlying a super-critical reaction zone.

We adopt a porous flow model to describe the flow across a two-dimensional square domain of height $H=1.5$ km and length $L=1.5$ km (Fig. 3). The base of the system is impermeable and isothermal. The temperature difference across the layer is ΔT and is set to vary from 400 to 600 °C. Fluid flow enters the top of the model at 2 °C and vents with a zero vertical temperature gradient. The top of the system is permeable and at a constant pressure (300 bars) so that the velocity is vertical at the top interface. The vertical sides of the system are impermeable and are planes of symmetry for the temperature and flow fields (i.e., the fluid velocity is parallel to the interfaces and there is no heat conduction across them). We assume the flow obeys Darcy's law (Eq. (1)) which in two-dimensions reduces to

$$\begin{aligned} -\frac{k}{\mu}u &= \frac{\partial p}{\partial x} \\ -\frac{k}{\mu}w + \rho g &= \frac{\partial p}{\partial z} \end{aligned} \tag{3}$$

where x and z (positive downwards) designate the cartesian coordinates, and u and w are the horizontal and vertical components of the Darcy velocity, p is the fluid pressure, g is the gravitational acceleration, ρ and μ are the fluid density and viscosity, respectively.

Neglecting the transient density variations, the continuity equation is

$$\frac{\partial(\rho u)}{\partial x} + \frac{\partial(\rho w)}{\partial z} = 0 \tag{4}$$

We define the stream function Ψ

$$\begin{aligned} \frac{\partial \Psi}{\partial z} &= \rho u \\ \frac{\partial \Psi}{\partial x} &= -\rho w \end{aligned} \tag{5}$$

Eliminating pressure by taking the curl of Eq. (3) leads to

$$\frac{1}{R}\nabla^2\Psi = -\left(\frac{\partial}{\partial x}\left(\frac{1}{R}\right)\frac{\partial \Psi}{\partial x} + \frac{\partial}{\partial z}\left(\frac{1}{R}\right)\frac{\partial \Psi}{\partial z}\right) - \frac{\partial(\rho_f)}{\partial x} \tag{6}$$

where R is the hydraulic resistivity

$$R = \frac{k\rho g}{\mu} \tag{7}$$

Assuming that the fluid and the rock are in thermal equilibrium the heat transfer equation is

$$(\rho c)_{eq}\frac{\partial T}{\partial t} + (\rho c)_f \nabla\cdot(\boldsymbol{q}T) = \lambda_{eq}\nabla^2 T \tag{8}$$

where $(\rho c)_{eq}$ and $\lambda_{eq}=2.5$ W/m K are the volumetric heat capacities and thermal conductivity of the fluid saturated porous medium, respectively, $(\rho c)_f=4.2\times10^6$ J/K m^3 is the volumetric heat capacities of the fluid, T is the temperature and $\boldsymbol{q}(u,w)$ is Darcy velocity vector. Since the ratio $\gamma=(\rho c)_f/(\rho c)_{eq}$ is close to unity, the thermal diffusivity of the fluid saturated porous medium can be approximated by $\kappa=(\lambda)_{eq}/(\rho c)_f=6\times10^{-7}$ m^2/s. The temperature- and pressure-dependent fluid density is obtained from lookup tables that were constructed using the equation of state of Pitzer et al. [38] at temperatures <300 °C and Anderko and Pitzer [39] at temperature >300 °C. We have verified that these densities are very similar to those predicted by the more recent equation of state of Berndt et al. [34]. The viscosity of the hydrothermal fluid is temperature- and pressure-dependent and derived using the relationship of Meyer et al. [40].

The problem is non-dimensionalized by scaling lengths with H, time with H^2/κ, temperature with ΔT, velocities with κ/H. In their dimensionless form the temperature (θ) and stream function (Ψ) equations are

$$\frac{\partial\theta}{\partial\tau} + \nabla\cdot(\boldsymbol{q}\theta) = \nabla^2\theta \tag{9}$$

$$\begin{aligned} &\frac{1}{r}\nabla^2\Psi = -\left(\frac{\partial}{\partial x}\left(\frac{1}{r}\right)\frac{\partial \Psi}{\partial x} + \frac{\partial}{\partial z}\left(\frac{1}{r}\right)\frac{\partial \Psi}{\partial z}\right) + Ra\left(\frac{\partial(\chi(\theta,\Pi))}{\partial x}\right) \\ &Ra = \frac{\Delta\rho g H k_o}{\mu_o\kappa};\ \chi(\theta,\Pi) = -\left(\frac{\rho(T,P)-\rho_o}{\Delta\rho}\right) \end{aligned} \tag{10}$$

where $\Delta\rho$ is the density contrast between hot and cold fluids and μ_o and ρ_o are the viscosity and density at the bottom of the system, respectively. When the bottom temperature is 600 °C, $\Delta\rho=910$ kg/m^3, $\mu_o=5.1\times10^{-5}$ Pas and $\rho_o=130$ kg/m^3. k_o is the permeability reference at the top of the system, $r = R/R_o$ ($R_o = k_o \rho_o g/\mu_o$) is the dimensionless resistivity, χ is a dimensionless function that scales the density variations and Π is the dimensionless pressure and satisfies

$$\Pi = \frac{k_o}{\mu_o \kappa}(p - \rho_o g z) \qquad (11)$$

Ra is the Rayleigh number and describes the vigor of convection. *Ra* varies linearly with the permeability which is the free parameter in our problem. Because the amplitude of *Ra* depends on the fluid properties at the base of the system, it is difficult to compare meaningfully *Ra* numbers for solutions computed at different basal temperatures. Therefore, we also parameterize the vigor of convection with the Nusselt number *Nu* which for $H = L$ can be written

$$Nu = -\int_0^1 \frac{\partial \theta}{\partial z}\bigg|_{z=0} \mathrm{d}x \qquad (12)$$

which represents the ratio of the observed vertical heat transport to that which would occur by conduction alone.

The equations are discretized on an $n \times n$ points ($n = 128$, 256 or 384) staggered grid. The temperature and stream function points are located in the centers and at the corners of the cells, respectively; the vertical and horizontal velocities are located in the middle of the horizontal and vertical cell sides, respectively. The temperature (Eq. (9)) is solved by an alternative direction implicit finite difference scheme [41]. This routine has been tested successively and used to solve various convective problems [e.g., [42,43]]. The stream function is solved using the following spectral decomposition:

$$\Psi(x,z) = \sum_{i=1,n}\sum_{j=1,l} \Psi_{i,j} \sin(i\pi x)\cos\left((2j+1)\frac{\pi z}{2}\right) \qquad (13)$$

This decomposition is valid for a two-dimensional flow in a box with impermeable vertical boundaries but with a top where the fluid is free to leave or enter [42,43].

3. Results

3.1. Uniform permeability models

We first ran a series of models with a uniform permeability field throughout the two-dimensional domain. Fig. 4 shows the results for a model with $Nu = 7.5$, $k_o = 1.8 \times 10^{-15}$ m^2 and a basal temperature of 600 °C (see Table 1 for model parameters). Results for several other models are summarized in Table 1. The circulation (Fig. 4a) consists of three upflow and two downflow zones and the venting temperature is ~330 °C. The neutral density (Fig. 4b) decreases from 800 kg/m^3 at the top of the system to 600–650 kg/m^3 at the top of the bottom thermal boundary layer and reaches a minimum (~200 kg/m^3) in the thermal boundary layer where the flow is essentially horizontal.

In order to constrain the salinity of neutrally buoyant fluids in the upflow zone we use the vertical pressure and temperature profiles along the axis of the upflow zone located on the left side of the box to compute the densities of fluids with salinities ranging from 5 to 15 wt.%. These vertical density profiles are calculated using the equation of state of Berndt et al. [34] for the system H_2O–NaCl. We then compare these density profiles with the local neutral densities along the same profile in the model to determine the maximum salinity of fluids that would rise through the whole upflow zone (Fig. 4c). We equate this to the maximum feasible venting salinity. The neutral densities increase throughout the whole upflow zone (Fig. 4c). At the base of the upflow zone (from 400 bars to ~390 bars), the neutral density increases rapidly from ~200 kg/m^3 to ~600 kg/m^3 because of the high-temperature gradients in the boundary layer. Throughout most of the upflow zone (from ~390 bars to ~310 bars), the neutral densities increase upwards only slowly because the temperature gradients are small. Close to the surface (from ~310 bars to 300 bars) the neutral density increases more rapidly as a result of near surface cooling caused by lateral conductive exchange between fluids flowing in and out of the system.

A large part of the upflow zone is in the two-phase area. However, this is likely a result of the relatively low Nusselt number experiments that we are running. The permeability $k_o \sim 1.8 \times 10^{-15}$ m^2 is 1–2 orders of magnitude lower than the estimated permeability for black smoker fields [44–46]. Our results show that when the permeability increases, the depth to the two-phase zone increases (Table 1) because the depth to any given isotherms increases as the thickness of the bottom boundary layer decreases and temperatures along the axis of the upflow zone become more isothermal [37]. As we will discuss in more detail in Section 4 it is likely that for permeability and Nusselt more typical of mid-ocean ridge hydrothermal systems only the reaction zone is in the two-phase area while most of the upflow zone is single-phase.

In the single-phase portion of the constant permeability solutions, the maximum salinity of upwelling fluids is ~12–15 wt.% NaCl (Fig. 4c and Table 1). Schoofs and Hansen [47] who investigated the problem of the depletion of a brine layer that has returned to the single-phase area also found that fluid with similar salinities could potentially rise in mid-ocean ridge hydrothermal systems. The maximum salinity predicted by our models

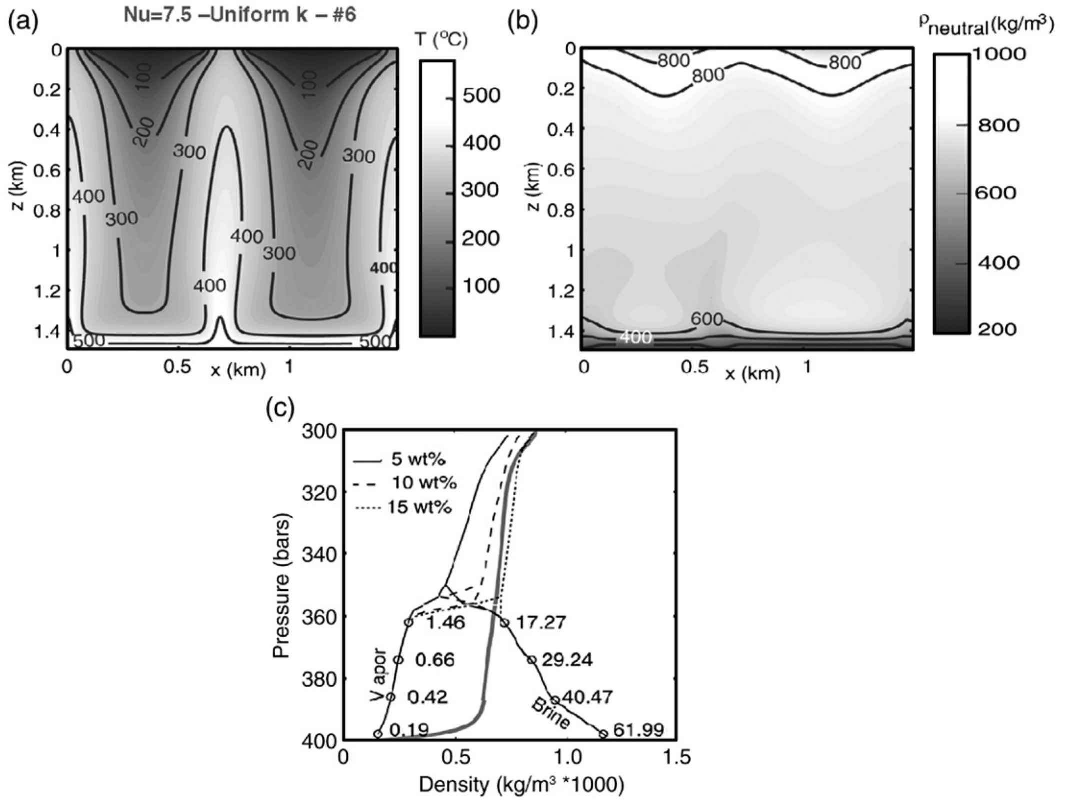

Fig. 4. (a) Two-dimensional temperature field for a model with a uniform permeability structure. The system is 1.5 km deep and 1.5 km wide. The model parameters can be found in Table 1 (model 6). The solution has a maximum venting temperature of 332 °C. (b) Two-dimensional distribution of neutral densities for the model shown in (a). Note that the presence of two 800 kg/m^3 contours near the seafloor is a result of non-linear fluid properties. The pressure gradients in the downflow zone are highest just below the seafloor where the fluids are still cold enough to have densities that are close to inflowing seawater but have warmed up enough that their viscosity is reduced substantially. (c) Comparison between the local neutral density at the axis of the upflow zone (thick gray line) of the model shown in (a) and (b), and the density of fluids with salinities of 5 (thin solid line), 10 (dashed line) and 15 (dotted line) wt.% NaCl. A large part of the upflow zone is in the two-phase area where each of the density curves splits into two lines representing the densities of the coexisting vapor and brine phases. Numbers on these lines refer to the salinity of the two phases at different pressures in the upflow zone. In the single-phase area fluids with salinities up to 12–13 wt.% NaCl can rise to the surface.

is also close to the maximum salinity of fluids trapped in the dike section (i.e., 13 wt.% NaCl [22]) but exceeds the maximum salinity of fluids observed in modern vents. In Fig. 2b, diamond symbols show the predicted maximum venting density as a function of venting temperature for experiments with a uniform permeability field and with various bottom temperatures (500 and 600 °C), Rayleigh (200 to 800) and Nusselt numbers (2.2 to 7.5). These densities always significantly exceed the maximum observed densities of venting fluids.

3.2. Influence of the pillow–dikes interface

The permeability of the crust is known to increase by several orders of magnitude from the sheeted dike complex to the pillow lava layer [e.g., [48]]. We ran a series of simulations in which we included a high-permeability layer in the upper 410 m of the model to simulate the effect of the extrusive layer 2A overlying an intrusive layer 2B. In Fig. 5 we show the results for a permeability contrast of 10 and a basal temperature of 600 °C.

The presence of the permeability interface leads to a narrowing of the upflow zone in the upper layer (Fig. 5a). As the flow concentrates in the lower layer, the vertical pressure gradients and thus the neutral densities increase below the interface (Fig. 5b). When the flow crosses the interface and enters the high-permeability upper layer the pressure gradients decrease sharply and the neutral densities decrease. As the fluid moves up away from the interface the neutral densities increase as the upflow zone narrows and the fluids cool down.

For a permeability contrast of 10 (Fig. 5), the inferred maximum venting salinities decrease to about 11 wt.% NaCl (Fig. 5b). As the permeability contrast increases,

Table 1
Summary of the parameters and results for the numerical experiments

Model #	Parameters								Results					
	T_b (°C)	k_o ($\times 10^{-15}$ m^2)	$k_{r,d}$	w_u (m)	$k_{r,u}$	w_s (m)	h_s (m)	$k_{r,s}$	Nu	T_v (°C)	S_{max} (wt.%)	ρ_{max} (kg/m^3)	$P_{2\psi}$ (bars)	$(\Delta P/\Delta T)_{max}$ (bars/°C)
Uniform														
1	500	0.5	–	–	–	–	–	–	2.2	323	15.5	867	385	1.3
2	500	0.7	–	–	–	–	–	–	3.1	283	13.1	894	390	1.3
3	500	1.5	–	–	–	–	–	–	4.5	239	12.0	934	400	1.3
4	600	0.4	–	–	–	–	–	–	3.3	392	14.5	761	310	0.9
5	600	1.0	–	–	–	–	–	–	5.7	360	13.3	793	340	0.9
6 (Fig. 4)	600	1.8	–	–	–	–	–	–	7.5	332	12.2	814	355	1.0
2-layer														
7 (Fig. 5)	600	0.52	10	–	10	–	–	10	3.1	249	10.9	923	362	6.9
8	600	0.22	100	–	100	–	–	100	2.6	170	7.30	966	370	14.6
Clogged-shell														
9	600		100	60	100	115	410	0.5	2.0	255	4.80	859	355	9
10 (Fig. 6)	600	0.22	100	60	100	115	410	0.1	2.0	285	4.00	810	355	7.2
11	600	0.22	100	60	10	115	410	0.5	2.0	295	10.3	856	350	5.3
12 (Fig. 7)	600	0.22	100	60	10	115	410	0.1	2.0	310	8.10	814	350	4.9
13	600	0.22	100	60	10	230	410	0.5	2.0	340	8.63	775	340	4.3
14	600	0.22	100	60	10	230	820	0.5	2.0	350	8.32	755	335	4.6
15	600	0.66	100	60	10	230	820	0.1	4.6	350	5.6	717	350	3
16 (Fig. 8)	600	2.20	100	60	10	230	820	0.1	14	350	6.40	724	395	1.5

Model parameters are described in Fig. 3. For results the symbols are as follows: Nu — Nusselt number (Eq. (12)); T_v — maximum venting temperature; S_{max} — maximum venting salinity; ρ_{max} — maximum venting density; $P_{2\psi}$ — pressure above which the system is in the two-phase area; $(\Delta P/\Delta T)_{max}$ is the maximum of $\partial P/\partial T$ in the shallow part of the upflow zone.

the maximum salinity of rising fluids decreases. For a permeability contrast of 100 (Table 1) fluids with salinities greater than 8–9 wt.% NaCl cannot cross the permeability interface.

These models suggest that systems with a high-permeability upper layer and a permeability contrast of at least 100 are reasonably consistent with the maximum observed venting salinities (Fig. 2b). However, as the upwelling plume narrows upon entering the high-permeability layer, it undergoes increased conductive cooling. In our models, a permeability contrast of 100 and a basal temperature of 600 °C leads to a venting temperature of only 170 °C (Table 1). This result is consistent with previous studies employing cellular

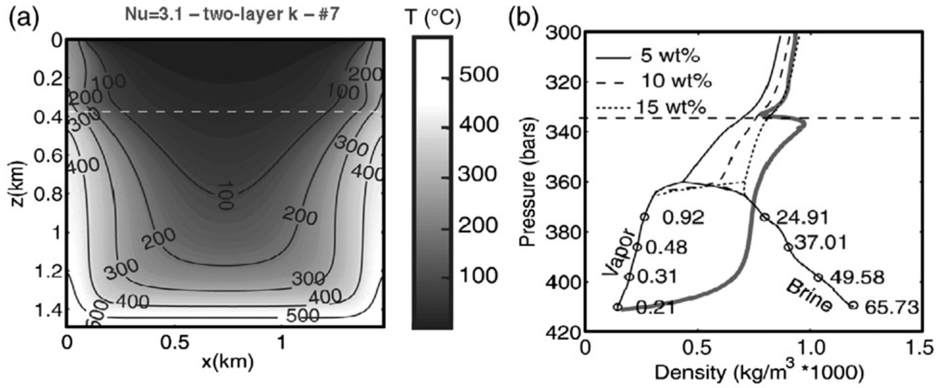

Fig. 5. (a) Two-dimensional temperature field for a model with a layered permeability field. The model parameters can be found in Table 1 (model 7). (b) Same as Fig. 4c but for the model shown in (a). The maximum venting temperature is 249 °C. The predicted maximum venting salinity is <11 wt.% NaCl. The permeability interface acts as a brine filter but also reduces the venting temperature and models with a reasonable permeability contrast cannot reproduce the temperatures of smokers (see Table 1, models 7 and 8).

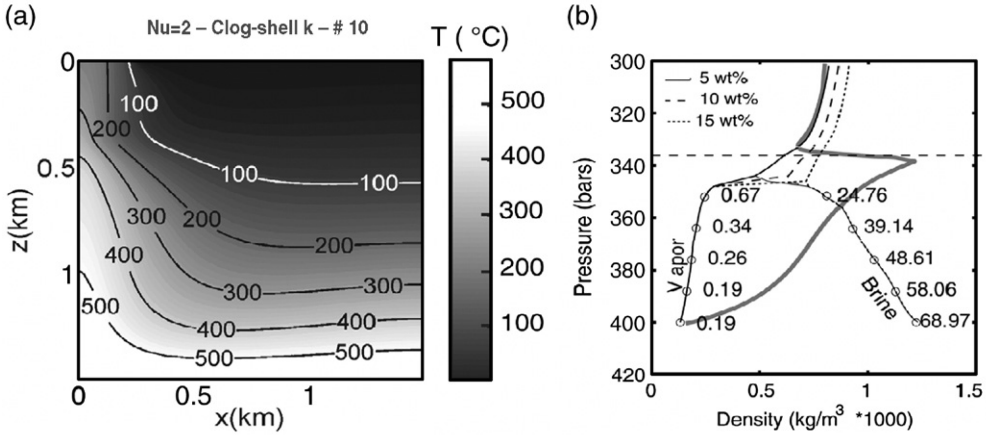

Fig. 6. Same as Fig. 5 but for a model with a clog-shell permeability structure. The model parameters can be found in Table 1 (model 10). The maximum venting temperature is ~285 °C and the maximum predicted maximum venting salinity is ~4 wt.% NaCl. The presence of the shell insulates the upflow zone and leads to venting temperature consistent with smoker activity. However, venting temperatures do not exceed 300 °C.

convection [37] and pipe models [49] both of which concluded that a high-permeability upper layer decreases venting temperature substantially. Thus, we infer that the two-layer permeability model cannot explain both the maximum venting salinity and temperature of smokers.

3.3. Clogged-shell permeability model

On the basis of observations in the stockworks of the Troodos ophiolite Cann and Strens [50] argue that the upflow zone of mid-ocean ridge hydrothermal systems is enclosed by a low-permeability shell formed by mineral alteration and precipitation in zones where hot fluids cool conductively and mix with seawater. The presence of such a shell will increase venting temperatures by insulating the upflow zone [37]. Drilling at the TAG hydrothermal mound confirms the importance of anhydrite precipitation in the region surrounding the highest temperature upflow [51,52]. The mixing between deep-seated, high-temperature, sulfate-free upwelling fluids and cooler, sulfate-rich seawater is known to lead to massive anhydrite ($CaSO_4$) precipitation at temperatures ranging from 100 °C to 250 °C [53]. Models of flow suggest that they will result in impermeable barriers between zones of focused hydrothermal discharge and broader recharge areas [43,54].

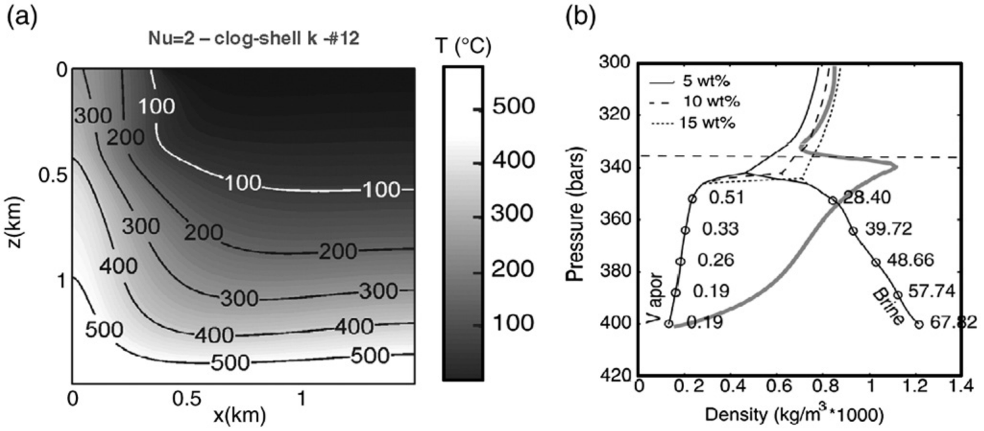

Fig. 7. Same as Fig. 5 but for a system in which the permeability contrast between the upper and lower parts of the upflow zone has been reduced to 10. The model parameters can be found in Table 1 (model 12). The maximum venting temperature and salinity are ~310 °C and 8.1 wt.% NaCl, respectively. The reduction of the permeability contrast between the top and bottom of the upflow zone leads to higher venting temperatures compared to the experiments shown in Fig. 6. The predicted venting salinity decreases as the permeability of the shell decreases and is reasonably consistent with the observations (Fig. 2).

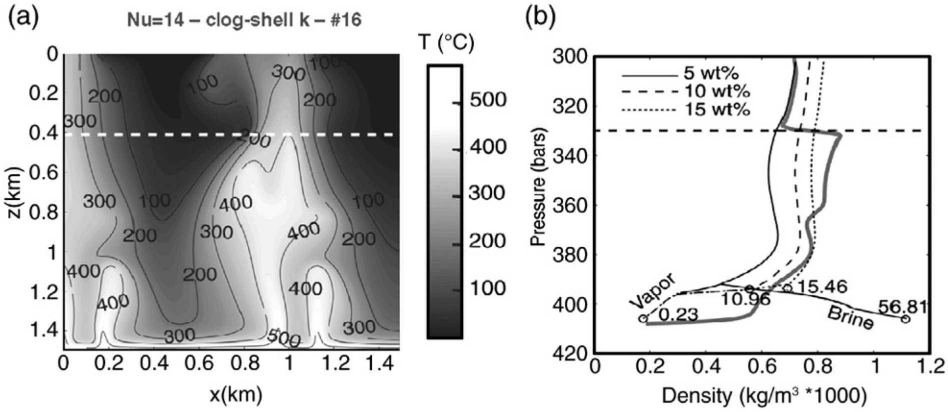

Fig. 8. (a) Same as Fig. 7 but for a model where *Nu* = 14. Other model parameters can be found in Table 1 (model 16). The circulation is composed of 2 upwelling and 2 downwelling regions and is unsteady. The two-phase area is limited to the deeper parts of the system close to the boundary layer. The temperature of the upflow zone ranges from 400 to 450 °C just above the bottom boundary layer to 350 °C at the seafloor. This temperature distribution is similar to the geochemically inferred thermal structure mid-ocean ridge hydrothermal systems [e.g., [5,6]]. The predicted maximum venting salinity is 6.4 wt.% NaCl and is consistent with observations.

Lowell et al. [54] use a simplified mixing model to estimate that the width of the impermeable anhydrite shells will range from 1 to 100 m.

To investigate the effect of adding a low-permeability shell to the two-layer model we ran a series of simulations using the permeability structure shown in Fig. 3. We first considered models in which we set the permeability contrast between the top and bottom of the system to 100. We included a low-permeability shell on the right hand side of the upflow zone located on the left side of the box. The shell is ~115 m wide and extends from the surface to the permeability interface (at a depth of 410 m). When the permeability of the shell is a factor of 1000 (Fig. 6) lower than the permeability of the upper layer, exit temperatures reach 285 °C which is substantially higher than the venting temperature of 170 °C obtained without the shell. The maximum inferred salinities are ~4 wt.% NaCl. This salinity is only slightly lower than the observed maximum salinity for temperatures exceeding ~270 °C but is substantially lower than the maximum salinities observed at lower temperature (Fig. 2a). The inclusion of the low-permeability shell leads to warmer upwelling temperatures but this also decreases the hydrostatic gradient (i.e., the neutral density) which leads to the relatively low maximum inferred salinities.

Since decreasing the permeability contrast between the upper and lower layers in a simple two-layer model leads to higher predicted venting salinities (Table 1) we considered a series of models in which we kept the impermeable shell but decreased the permeability of the portion of layer 2A within the upflow (Table 1). Such a decrease could result from mineral (sulfides) precipitation as the hot upwelling fluid cools while entering the high-permeability layer. Fig. 7 shows a model that is the same as that of Fig. 6 except that the permeability contrast between the bottom and upper layers is reduced to 10 in the upflow zone. The venting temperature and salinity are ~310 °C and 8.1 wt.% NaCl, respectively. As the permeability of the shell decreases the upflow zone is better insulated and venting temperatures increase while venting salinities decrease (compare models 11 and 12 in Table 1).

To evaluate this model further we ran a series of simulations in which we varied the width and height of the low-permeability zone (Table 1). Increasing the width and height of the low-permeability shell enhances the insulating effect leading to higher venting temperatures and lower venting salinities. For example for a 230 m-wide shell predicted maximum venting salinities are ~8.6 wt.% NaCl and the venting temperature is ~340 °C. When the height of the shell is increased to 820 m the venting temperatures and salinities are about 350 °C and ~8.3 wt.% NaCl, respectively. Such models are in reasonable agreement with the observations.

4. Discussion

In this paper we have examined the effect of permeability on the maximum salinity of mid-ocean ridge high-temperature hydrothermal vents. The results suggest that specific conditions are required to match the observed maximum salinities and the temperatures of smokers. First, the crust must have a layered permeability structure with a higher-permeability upper layer. The transition between the two layers acts as a "filter" impeding the ascent of high-salinity fluids. Second, a low-permeability shell must surround the high-temperature upflow zone. This shell formed by mineral precipitation insulates the upflow zone and favors the formation of high-temperature vents. Third, a decrease of the permeability in the upflow region of the extrusive layer in the shell model increases both the venting temperature and maximum salinities and yields the best fit to the observations for the models we have examined.

One major limitation of our model is the low Nusselt number obtained during the experiments. In most of our clogged-shell experiments (Table 1), the Nusselt number is 2 because the permeability k_o of the deep part of these models is fairly small ($k_{r,d}=2.2\times10^{-16}$ m^2) compared to the inferred permeability of active black smoker systems ($\sim10^{-12}$–10^{-13} m^2, e.g., [44–46]). Natural mid-ocean ridge hydrothermal systems are likely to have Nusselt numbers ranging from 5 to 100 [55]. Our experiments are limited to these low Nusselt numbers for computational reasons. The clogged-shell experiments include steep spatial permeability variations. The spectral technique used to solve the stream function equation is sensitive to these permeability variations and a fine grid is required to avoid classical aliasing problems that lead to numerical divergence. For a model with a 256 × 256 grid we can run stable solutions for Nusselt numbers up to ∼4.6 (Table 1). For higher *Nu* numbers a finer grid is required to resolve steep gradients in the temperature and stream function.

One critical consequence of such low Nusselt number experiments is that the temperature structure of the upflow zone in our models differs from the inferred structure of natural systems. Geochemical analyses of black smoker hydrothermal vents indicate that fluids leave the reaction zone at a temperature ∼400–450 °C and cool only by a few tens of °C before venting [5,6]. In contrast, the 450 °C-isotherm in our model with a Nusselt number of 2 is located at a depth of only ∼600 m (Figs. 6 and 7). As *Nu* increases the depth to this isotherm increases as the bottom boundary layer thins and the temperatures in the upflow zone become more isothermal (compare $P_{2\psi}$ of models 4–6 in Table 1). Thus, super-critical phase separation is restricted to the bottom boundary layer at high *Nu*. This is likely to change the distribution of the neutral densities in the upflow zone and may influence the predicted maximum venting salinities.

In order to test this hypothesis, we ran a few experiments with higher Nusselt numbers (Table 1). Fig. 8 shows the results of a simulation on a 384 × 384 grid for a model with the same configuration as that of Fig. 7 except that the impermeable shell extends to 820 m. The Nusselt number is 14 and $k_o=2.2\times10^{-15}$ m^2. At this high Nusselt number, the circulation comprises two upwelling and two downwelling regions and the flow is unsteady. The temperature distribution in the upflow zone on the left side is very similar to the geochemically inferred temperature distribution [5,6]. In this upflow zone, the depth to the 450 °C-isotherm is about 1200 m and is very close to the top of the thermal boundary layer (Fig. 8). Temperatures consistent with phase separation are limited to a region corresponding roughly to the thermal boundary layer. During the simulation, the time-dependent venting temperatures varied from ∼320 °C to ∼350 °C. When the venting temperature is ∼350 °C the predicted venting salinity is <7 wt.% NaCl. We infer that the predicted venting temperature and maximum salinity are not strongly dependent on the Nusselt number.

We also assume that the flow is laminar and can be represented by Darcy's law. This approximation may be adequate for the dike layer where the flow will be in narrow cracks [56,57] but likely breaks down in the large voids between pillows in the extrusive layer. When the flow becomes turbulent, Darcy's law for laminar flow should then be replaced by a quadratic drag law [58]. One critical consequence of such a change in the flow law is that the permeability contrasts we envision between the top and bottom of the system would not equate to a change in flow rate of the same amplitude since the pressure head–flow rate relationship is no longer linear. Thus, the contrast in permeability required to "filter" high-salinity brines may be larger than we predict.

Our models fit the observations when the width of the low-permeability shell is about 200 m. This value is higher than the 1 to 100 m inferred by Lowell et al. [54] based on a single-phase pipe model. Given the simplifications inherent to both models this difference is probably not significant. While our results show that the presence of a low-permeability upper layer and an impermeable shell can reproduce the temperature and maximum venting salinities of smoker fluids, the predicted dimensions of the shell and permeability contrast between the different regions undoubtedly have significant uncertainties. Good fits can also be obtained with somewhat narrower and less permeable shells.

One interesting implication of the change in permeability at the layer 2A/2B interface is that it might promote phase separation. In Table 1 we report the maximum value of $\partial P/\partial T$ in the shallow part of the upflow zone. In the two-layer and clog-shell experiments the permeability contrast between layers 2A and 2B leads to an increase in the maximum value of $\partial P/\partial T$ at the interface which moves local pressure–temperature conditions towards the two-phase curve. Since the increase in gradients is only a few bars/°C (Table 1), phase separation will occur only if the pressure–temperature conditions away from the interface are close to the critical/Clapeyron curve of the upwelling fluids.

Our models predict that fluids with salinities higher (up to 12–15 wt.% NaCl) than the maximum salinity observed in modern systems could be vented by a system in which the permeability of the upflow zone is uniform. This might happen if phase separation occurs in the pillow layer or if tectonic/diking events temporarily open high-permeability pathways from deep in the crust to the seafloor. Although the pressure conditions typical of the upper part of mid-ocean ridge hydrothermal systems (250–300 bars) may limit the salinity of brines produced in the pillows to 7–8 wt.% NaCl [14], fluids with salinity of 12–15 wt.% NaCl and up to 30 wt.% NaCl are commonly observed in shallow arc and back-arc systems [59,60]. We note that 16–26 wt.% NaCl fluids have been found in some fluid inclusions of the TAG mound [61] and postulate that they may be associated with a diking or tectonic event. Future time series obtained by mid-ocean ridge observatories should considerably improve our knowledge of the temporal links between venting salinities, temperatures and tectonic/diking events.

The models we have developed clearly include significant simplifications of the real systems. As we have noted above, the single-phase formulation cannot fully simulate flow in a super-critical reaction zone although we infer it is likely adequate in the upflow zone if the flow is single-phase. We use seawater properties (3.2 wt.% NaCl) to calculate the pressure–temperature conditions in the upflow zone and to derive neutral densities. The upflow of a fluid with a different salinity may change the pressure–temperature conditions in a manner that is difficult to quantify. The presence of two-phase flow in the upflow zone may also modify the pressure gradients determined. Thus, while our model provides physical insight into the expected buoyancy of fluids of various salinities in models with different permeability configurations, the precise details of the best fitting models are likely influenced by these assumptions. As two-phase algorithms [e.g., [62]] become available, they should be used to test our inferences and refine the constraints placed on the subsurface permeability structure by the temperatures and salinities of hydrothermal vents.

5. Conclusions

In this study we present a model that predicts the maximum salinity of mid-ocean ridge high-temperature hydrothermal systems. We assume that maximum venting salinity is controlled by the maximum density of fluids that are buoyant throughout the upflow zone. Using a numerical model of single-phase hydrothermal circulation we equate the neutral density $\rho_{\text{neutral}}=\frac{1}{g}\frac{\partial p}{\partial z}$ to the maximum salinity of rising fluids. We find that the permeability structure of the crust plays a critical role in determining the salinity and temperature of venting fluids. Models that can reproduce both the temperature and salinity of smokers require the presence of a permeability interface between the top (layer 2A) and bottom (layer 2B) of the system and a low-permeability shell between the upflow and downflow. Our model also fits the observations slightly better if the permeability of layer 2A is reduced in the upflow zone. While the permeability interface acts as a filter impeding the venting of high-salinity fluids, the low-permeability walls “thermally insulate” the upflow zone. Although the preferred permeability structure is quite complicated, it is consistent with the geological structure and inferences regarding permeability of the mid-ocean crust. The low-permeability shells have been observed in ophiolites and form by the precipitation of minerals in the regions where hot and cold fluids meet. The reduction of the permeability in the upflow region of layer 2A could result from mineral precipitation and alteration as the hot fluid cools down near the seafloor.

Acknowledgements

We thank Joe Cann, Meg Tivey, Deborah Kelley and Marv Lilley for helpful discussions and two anonymous reviewers for their thorough reviews of earlier versions of this manuscript. Publication of this work was supported by grant OCE-0243395 from the National Science Foundation.

References

[1] C.R.D. Lister, On the thermal balance of a mid-ocean ridge, Geophys. J. R. Astron. Soc. 26 (1972) 515–535.

[2] D.L. Williams, R.P. Von Herzen, J.G. Sclater, R.N. Anderson, The Galapagos spreading center: lithospheric cooling and hydrothermal circulation, Geophys. J. R. Astron. Soc. 38 (1974) 587–608.

[3] R.N. Anderson, M.A. Hobart, The relation between heat flow, sediment thickness, and age in the eastern Pacific, J. Geophys. Res. 81 (1976) 2968–2989.

[4] A. Schultz, J.R. Delaney, R.E. McDuff, On the partitioning of heat flux between diffuse and point source seafloor venting, J. Geophys. Res. 97 (1992) 12299–12314.

[5] W.E. Seyfried Jr., K. Ding, M.E. Berndt, Phase equilibria constraints on the chemistry of hot spring fluids at mid-ocean ridges, Geochim. Cosmochim. Acta 55 (1991) 3559–3580.

[6] W.E. Seyfried Jr., K. Ding, in: S.E. Humphris, et al., (Eds.), Seafloor Hydrothermal Systems: Physical, Chemical, Biological Interactions Within Submarine Hydrothermal Systems, Geophys. Monogr. Ser., vol. 91, AGU, Washington D.C., 1995, pp. 248–272.

[7] D.A. Butterfield, K.K. Roe, M.D. Lilley, J.A. Huber, J.A. Baross, R. W. Embley, G.J. Massoth, Mixing, reaction and microbial activity in the sub-seafloor revealed by temporal and spatial variation in diffuse flow vents at axial volcano, in: W.S.D. Wilcock, et al., (Eds.), The Subseafloor Biosphere at Mid-ocean Ridges, Geophys. Monogr. Ser., vol. 144, AGU, Washington D.C., 2004, pp. 269–290.

[8] M.K. Tivey, S.E. Humphris, G. Thompson, M.D. Hannington, P. A. Rona, Deducing patterns of fluid flow and mixing within the TAG active hydrothermal mound using mineralogical and geochemical data, J. Geophys. Res. 100 (1995) 12,527–12,555.

[9] M.J. Cooper, H. Elderfield, A. Schultz, Diffuse hydrothermal fluids from Lucky Strike hydrothermal vent field: evidence for a shallow conductively heated system, J. Geophys. Res. 105 (2000) 19,369–19,376.

[10] E.T. Baker, C.R. German, On the global distribution of hydrothermal vent sites, in: C.R. German, et al., (Eds.), Mid-ocean Ridges: Hydrothermal Interactions Between the Lithosphere and Oceans, Geophys. Monogr. Ser., vol. 148, AGU, Washington D.C., 2004, pp. 245–266.

[11] T.E. Jupp, A. Schultz, A thermodynamic explanation for black smoker temperature, Nature 403 (2000) 880–883.

[12] K.L. VonDamm, Control on the chemistry and temporal variability of seafloor hydrothermal fluids, in: S.E. Humphris, et al., (Eds.), Seafloor Hydrothermal Systems: Physical, Chemical, Biological and Geological Interactions, Geophys. Monogr. Ser., vol. 91, AGU, Washington D.C, 1995, pp. 222–247.

[13] D.A. Butterfield, W.E. Seyfried, M.D. Lilley, Composition and evolution of hydrothermal fluids, in: P.E. Halbach, et al., (Eds.), Energy and Mass Transfer in Submarine Hydrothermal Systems, Dahlem Workshop Report, vol. 89, Free University of Berlin, Berlin, 2003, pp. 123–161.

[14] J.R. Delaney, D.W. Mogk, M.J. Mottl, Quartz-cemented breccias from the Mid-Atlantic Ridge: samples of a high-salinity hydrothermal upflow zone, J. Geophys. Res. 92 (1987) 9175–9192.

[15] J. Cowan, J. Cann, Supercritical two-phase separation of hydrothermal fluids in the Troodos ophiolite, Nature 333 (1988) 259–261.

[16] K.L. VonDamm, Systematics and postulated controls on submarine hydrothermal solution chemistry, J. Geophys. Res. 93 (1988) 4551–4561.

[17] J.L. Bischoff, R.J. Rosenbauer, Salinity variations in submarine hydrothermal systems by layered double-diffusive convection, J. Geol. 97 (1989) 613–623.

[18] D.A. Butterfield, G.J. Massoth, R.E. McDuff, J.E. Lupton, M.D. Lilley, The geochemistry of hydrothermal fluids from the ASHES vent field, Axial Seamount, Juan de Fuca ridge: subseafloor boiling and subsequent fluid–rock interaction, J. Geophys. Res. 95 (1990) 12,895–12,922.

[19] D.A. Butterfield, R.E. McDuff, M.J. Mottl, M.D. Lilley, J.E. Lupton, G.J. Massoth, Gradients in the composition of hydrothermal fluids from the Endeavour segment vent field: phase separation and brine loss, J. Geophys. Res. 99 (1994) 9561–9584.

[20] F.J. Fontaine, W.S.D. Wilcock, The dynamics and storage of brines in mid-ocean ridges hydrothermal systems, J. Geophys. Res. 111 (2006) B06102, doi:10.1029/2005JB003866.

[21] R.O. Fournier, Conceptual models of brine evolution in magmatic–hydrothermal systems, USGS Prof. Pap. 1350 (1987) 1487–1506.

[22] P. Nehlig, Salinity of oceanic hydrothermal fluids: a fluid inclusion study, Earth Planet. Sci. Lett. 102 (1991) 310–325.

[23] D.S. Kelley, P.T. Robinson, J.G. Malpas, Processes of brine generation and circulation in the oceanic crust: fluid inclusion evidence from the Troodos Ophiolite, Cyprus, J. Geophys. Res. 97 (1992) 9307–9322.

[24] D.S. Kelley, K.M. Gillis, G. Thompson, Fluid evolution in submarine magma–hydrothermal systems at the mid-atlantic ridge, J. Geophys. Res. 98 (1993) 19579–19596.

[25] D.S. Kelley, G.L. Früh-Green, Volatile lines of descent in submarine plutonic environments: insights from stable isotope fluid inclusion analyses, Geochim. Cosmochim. Acta 65 (2001) 3325–3346.

[26] P.J. Saccocia, K.M. Gillis, Hydrothermal upflow zones in the oceanic crust, Earth Planet. Sci. Lett. 136 (1995) 1–16.

[27] A. McNabb, J. Fenner, Thermohaline convection beneath the ocean floor, Paper Presented at CSIRO/DSIR Seminar on Convective Flows in Porous Media, Dep. of Sci. and Ind. Res, Wellington, New Zealand, 1985.

[28] C.R. Faust, J.W. Mercer, Geothermal reservoir simulation 1. Mathematical models for liquid- and vapor-dominated hydrothermal systems, Water Resour. Res. 15 (1979) 23–30.

[29] S.E. Ingebritsen, D.O. Hayba, Fluid flow and heat transport near the critical point of H_2O, Geophys. Res. Lett. 21 (1994) 2199–2202.

[30] D.O. Hayba, S.E. Ingebritsen, Multiphase groundwater flow near a cooling plutons, J. Geophys. Res. 102 (1997) 12,235–12,252.

[31] W. Xu, R.P. Lowell, Oscillatory instability of one-dimensional two-phase hydrothermal flow in heterogeneous porous media, J. Geophys. Res. 103 (1998) 20,859–20,868.

[32] K.C. Lewis, R.P. Lowell, Mathematical modeling of phase separation of seawater near an igneous dike, Geofluids 4 (2004) 197–209.

[33] R.P. Lowell, L.N. Germanovich, Hydrothermal processes at mid-ocean ridges: results from scale analysis and single-pass models, in: Christopher R. German, et al., (Eds.), Mid-ocean Ridges: Hydrothermal Interactions Between the Lithosphere and Oceans, Geophys. Monogr. Ser., vol. 148, AGU, Washington D.C., 2004, pp. 110–127.

[34] M.E. Berndt, M.E. Person, W.E. Seyfried Jr., Phase separation and two-phase flow in seafloor hydrothermal systems: geophysical modeling in the $NaCl–H_2O$ system, Paper Presented at the Eleventh Annual V. M. Goldschmidt Conference, Geochem. Soc, Hot Springs, Va, 2001.

[35] W.S.D. Wilcock, A model for the formation of transient event plumes above mid-ocean ridge hydrothermal systems, J. Geophys. Res. 102 (1997) 12109–12122.

[36] T. Jupp, A. Schultz, Physical balances in subseafloor hydrothermal convection cells, J. Geophys. Res. 109 (2004) B05101, doi:10.1029/2003JB002697.

[37] W.S.D. Wilcock, Cellular convection models of mid-ocean ridge hydrothermal circulation and the temperatures of black smoker fluids, J. Geophys. Res. 103 (1998) 2585–2596.

[38] K.S. Pitzer, J.C. Peiper, R.H. Busey, Thermodynamic properties of aqueous sodium chloride solutions, J. Phys. Chem. Ref. Data 13 (1984) 1–106.

[39] A. Anderko, K.S. Pitzer, Equation-of-state representation of phase equilibria and volumetric properties of the system $NaCl–H_2O$ above 573 K, Geochim. Cosmochim. Acta 57 (1993) 1657–1680.

[40] C.A. Meyer, R.B. McClintock, G.J. Silvestri, R.C. Spencer Jr., ASME Steam Table: Thermodynamic and Transport Properties of Steam, Am. Soc. of Mech. Eng, New York, USA, 1993.

[41] J. Douglas, G.G. Rachford, On the numerical solution of heat conduction problems in two and three space variables, Trans. Am. Math. Soc. 82 (1956) 421–439.

[42] M. Rabinowicz, J. Boulègue, P. Genthon, Two and three-dimensional modeling of hydrothermal convection in the sedimented Middle Valley segment, Juan de Fuca Ridge, J. Geophys. Res. 103 (1998) 24045–24065.

[43] F.J. Fontaine, M. Rabinowicz, J. Boulègue, Permeability changes due to mineral diagenesis in fractured crust: implications for hydrothermal circulation at mid-ocean ridges, Earth Planet. Sci. Lett. 184 (2001) 407–425.

[44] R.P. Lowell, L.N. Germanovich, On the temporal evolution of high-temperature hydrothermal systems at ocean ridge crest, J. Geophys. Res. 99 (1994) 565–576.

[45] W.S.D. Wilcock, A. McNabb, Estimates of crustal permeability on the Endeavour segment of the Juan de Fuca mid-ocean ridge, Earth Planet. Sci. Lett. 138 (1995) 83–91.

[46] W.S.D. Wilcock, A.T. Fisher, Geophysical constraints on the subseafloor environment near mid-ocean ridges, in: W.S.D. Wilcock, et al., (Eds.), The Subseafloor Biosphere at Mid-ocean Ridges, Geophys. Monogr. Ser., vol. 144, AGU, Washington D.C., 2004, pp. 51–74.

[47] S. Schoofs, U. Hansen, Depletion of a brine layer at the base of ridge-crest hydrothermal systems, Earth Planet. Sci. Lett. 180 (2000) 341–353.

[48] A.T. Fisher, Permeability within basaltic oceanic crust, Rev. Geophys. 36 (1998) 143–182.

[49] A.R. Pascoe, J.R. Cann, Modeling diffuse hydrothermal flow in black smoker vent fields, in: L.M. Parsons, et al., (Eds.), Hydrothermal Vents and Processes, Geol. Soc. Spe. Pub., vol. 87, 1995, pp. 159–173.

[50] J. Cann, M.R. Strens, Modeling periodic megaplume emission by black smoker systems, J. Geophys. Res. 94 (1989) 12227–12237.

[51] M.K. Tivey, R.A. Mills, D.A.H. Teagle, Temperature and salinity of fluid inclusions in anhydrite as indicators of seawater entrainment and heating in the TAG active mound, Proc. Ocean Drill. Program Sci. Results 158 (1998) 179–190.

[52] Y. Fouquet, K. Henry, R. Knott, P. Cambon, Geochemical section of the TAG hydrothermal mound, Proc. Ocean Drill. Program Sci. Results 158 (1998) 363–387.

[53] J.L. Bischoff, W.E. Seyfried, Hydrothermal chemistry of seawater from 25 °C to 350 °C, Am. J. Sci. 278 (1978) 838–860.

[54] R.P. Lowell, Y. Yao, L.N. Germanovich, Anhydrite precipitation and the relationship between focused and diffuse flow in seafloor hydrothermal systems, J. Geophys. Res. 108 (2003), doi:10.1029/2002JB002371.

[55] W.S.D. Wilcock, J.R. Delaney, Mid-ocean ridge sulfide deposits: evidence for heat extraction from magma chambers or cracking fronts? Earth Planet. Sci. Lett. 145 (1996) 49–64.

[56] P. Nehlig, Fracture and permeability analysis in magma-hydrothermal transition zone in the Samail ophiolite (Oman), J. Geophys. Res. 99 (1994) 589–602.

[57] W.S.D. Wilcock, Physical response of mid-ocean ridge hydrothermal systems to local earthquakes, Geochem. Goephys. Geosyst. 5 (2004) Q11009, doi:10.1029/2004GC000701.

[58] D. Nield, D. Joseph, Effects of quadratic drag on convection in a saturated porous medium, Phys. Fluids 28 (1985) 995–997.

[59] V. Lüders, B. Pracejus, P. Halbach, Fluid inclusion and sulfur isotope studies in probable modem analogue Kuroko-type ores from the JADE hydrothermal field (Central Okinawa Trough, Japan), Chem. Geol. 173 (2001) 45–58.

[60] C. Lécuyer, M. Dubois, C. Marignac, G. Gruau, Y. Fouquet, C. Ramboz, Phase separation and fluid mixing in subseafloor back arc hydrothermal systems: a microthermometric and oxygen isotope study of fluid inclusions in the barite–sulfide chimneys of the Lau basin, J. Geophys. Res. 104 (1999) 17,911–17,927.

[61] N.S. Bortnikov, V.A. Simonov, Y.A. Bogdanov, Fluid inclusions in minerals from modern sulfide edifices: physicochemical conditions of formation and evolution of fluids, Geol. Ore Depos. 46 (2004) 64–75.

[62] S. Geiger, T. Driesner, C.A. Heinrich, S.K. Matthaï, On the dynamics of NaCl–H_2O fluid convection in the Earth's crust, J. Geophys. Res. 110 (2005) B07101, doi:10.1029/2004JB003362.

[63] J.C. Alt, Subseafloor processes in mid-ocean ridge hydrothermal systems, in: S.E. Humphris, et al., (Eds.), Seafloor Hydrothermal Systems: Physical, Chemical, Biological and Geological Interactions, Geophys. Monogr. Ser., vol. 91, AGU, Washington D.C, 1995, pp. 85–114.